Effect of Co concentration on cation distribution and magnetic and magneto-optical properties of $Co_xZn_{1-x}Fe_2O_4$ nanoparticles synthesized with citrate precursor method

Atul Thakur[1] , Irina Edelman[2,3] , Dmitriy Petrov[2,a] , Sergey Ovchinnikov[2,3] , Preeti Thakur[1] , Sergey Zharkov[2,3], Yuri Knyazev[2,3] , Alexander Sukhachev[2]

[1] Amity University Haryana, Gurugram, Haryana 122413, India
[2] Kirensky Institute of Physics, Federal Research Center KSC, Siberian Branch, Russian Academy of Sciences, 50 Akademgorodok, Krasnoyarsk 660036, Russia
[3] Siberian Federal University, 79 Svobodny Ave., Krasnoyarsk 660041, Russia
[a] Address all correspondence to this author. e-mail: irbiz@iph.krasn.ru

Magnetic properties of mixed spinel ferrites are determined, in great extent, by the magnetic cation distribution among tetrahedral and octahedral positions in a crystal. In the case of CoZn-ferrites, most researchers reported a predominant localization of the divalent cobalt ions in octahedral positions. Using the citrate precursor auto-combustion method, we successfully synthesized $Co_xZn_{1-x}Fe_2O_4$ nanoparticles (x changed from 0.0 to 0.5) with an approximately evenly distribution of Co^{2+} ions between these interstitial positions. Fe^{3+} ions are localized preferably in octahedral positions. This type of 3d-ion distribution predetermined the combination of the large saturation magnetization and very low coercive field of the nanoparticles, which may be of importance for applications. MCD spectra of $Co_xZn_{1-x}Fe_2O_4$ nanoparticles are studied here for the first time. Revealed intense MCD peak at 1.75 eV corresponds to the emission wavelength (710 nm) of some lasers, e.g., ALP-710 nm (NKT Photonics, Denmark) which may be of interest for photonic devices.

Introduction

Until very recently, mixed cobalt-containing spinel ferrites have been one of the central objects of magnetic materials research [1–9]. Among them, ferrites based on Zn and Co ($Co_xZn_{1-x}Fe_2O_4$) have attracted great attention from researchers and engineers due to their unique properties, such as high specific electrical resistivity, low eddy current losses [10, 11], high saturation magnetization and Curie temperature [12], and temperature stability and low cost [13]. Nanoparticles (NPs) with different relative Co and Zn concentrations have an impressive range of applications, such as systems for targeted drug delivery and hyperthermia [14–16], magnetic resonance imaging [17], magnetic fluids [18], water purification [19], catalysis [20, 21], and many others (see, for example, Rev. [22] and references). Due to the wide application of NPs, it is necessary to improve their properties, particularly their magnetic properties, which

determine the possibility of their use in many applications and depend primarily on the ratio of Co and Zn concentrations in the ferrite composition. The extreme members of the $Co_xZn_{1-x}Fe_2O_4$ series, $ZnFe_2O_4$ and $CoFe_2O_4$, have the same crystalline spinel structure as the Fd-3 m space group but differ in the cation distribution between crystalline positions. $ZnFe_2O_4$ is a normal spinel where divalent Zn^{2+} ions occupy tetrahedral positions and trivalent Fe^{3+} ions are situated in octahedral positions. $CoFe_2O_4$ refers to the partly inverse spinel structure where the Fe^{3+} and Co^{2+} ions occupy both tetrahedral and octahedral positions with an inversion parameter ranging from 0.6 to 0.9 [23, 24]. According to the cation distributions, $ZnFe_2O_4$ is characterized by antiferromagnetic order with a low Neel temperature $T_N = 10$ K. $CoFe_2O_4$ is a ferrimagnet with the Curie temperature T_c and the room temperature saturation magnetization M_s depending on the inversion parameter that can reach values

of 793 K and 66.3 A m^2/kg, correspondingly [12]. Great variations of the inversion parameter are frequently observed in the case of NPs due to low particle dimensions, surface effects, and high concentrations of surface defects [25]. Note that Zn-ferrite in the nanoparticle state can be partly inverted too. The degree of inversion in this case can be presented with the formula $(Zn_{1-\delta}Fe_\delta) [Zn_\delta Fe_{2-\delta}] O_4$, where parentheses and square brackets refer to tetrahedral and octahedral positions, respectively. For example, the authors of [25] synthesized partially inverted Zn-ferrite NPs with a size of 9.8 ± 0.2 nm using the thermal decomposition technique and showed that the obtained NPs were ferrimagnetic at room temperature with a saturation magnetization of 44.9 A m^2/kg. The same authors provided a table of saturation magnetization values obtained by 15 other authors for partially inverted Zn-ferrite NPs synthesized by various methods, which varied from 10 to 88 A m^2/kg. An even more complex distribution of cations across crystal positions can be expected for the case of mixed spinels $Zn_{1-x}Co_xFe_3O_4$ synthesized with different techniques. In Ref. [26], monophasic Co-ferrite, Zn-ferrite, and $Co_{0.5}Zn_{0.5}Fe_2O_4$ NPs were synthesized via a flash method based on urea decomposition. The mixed NPs were morphologically similar to the Co-ferrite NPs, and $Co_{0.5}Zn_{0.5}Fe_2O_4$ displayed an M_s of 55.3 A m^2/kg, which was lower than the M_s of Co-ferrite (66.3 A m^2/kg) but higher than the data for a mixed Zn-ferrite composition reported by other authors. For example, $Co_xZn_{1-x}Fe_2O_4$ NPs with x varying from 0 to 1.0 synthesized by the polyethylene glycol (PEG)-assisted hydrothermal route [27] demonstrated essentially lower M_s values of 7.83, 45.7, and 44.9 A m^2/kg for $x = 0.5$, 0.7, and 1.0, respectively. When studying the electrical and magnetic properties of $Co_{1-x}Zn_xFe_2O_4$ NPs with $x = 0$, 0.2, and 0.8 synthesized by combustion, the authors of Ref. [28] obtained M_s values of 56.72, 47.08, and 2.5 A m^2/kg for $CoFe_2O_4$, $Co_{0.8}Zn_{0.2}Fe_2O_4$, and $Co_{0.2}Zn_{0.8}Fe_2O_4$, respectively. High room temperature M_s values were demonstrated in Ref. [29] for $Co_xZn_{1-x}Fe_2O_4$ NPs with $x = 0.0$, 0.1, 0.2, 0.3, 0.4, and 0.5 synthesized by the combustion method: 10.01, 16.76, 34.88, 52.21, and 67.18 A m^2/kg, respectively. The dependence of unsteady M_s behavior on Co concentration was observed in Ref. [30] for $Co_xZn_{1-x}Fe_2O_4$ NPs with x varying from 1.0 to 0.5 synthesized from metal salts by co-precipitation of hydroxides. As the Co content decreased, the M_s increased, reached a value of 114 A m^2/kg, and then decreased again. However, it remained very high for $x = 0.5$–82 A m^2/kg. The reason for this behavior was not elucidated in the paper. These examples demonstrate the exceptionally strong effect of the technological methods on the properties of the synthesized NPs and stress the necessity of thoroughly investigating the magnetic characteristics of the obtained samples in each case.

A series of $Co_xZn_{1-x}Fe_2O_4$ NPs with x values varying from 0.0 to 0.5 prepared by the citrate precursor technique demonstrated remarkable resistivity and improved dielectric properties

[31]. In particular, the value of the dielectric loss tangent varied in the range of 0.003–0.052 at 1 MHz for different concentrations of cobalt ions; the samples were found to be good insulators with enormous resistivity values ranging from 1.4×10^{10} $\Omega \times cm$ to 1.4×10^{11} $\Omega \times cm$. The specific synthesis conditions that ensured such electrical characteristics could lead to a redistribution of Co^{2+}, Fe^{3+}, and Zn^{2+} cations between tetrahedral and octahedral positions in $Co_xZn_{1-x}Fe_2O_4$ nanocrystals and thus greatly affect their magnetic properties. In particular, they can allow the formation of magnetic properties necessary for specific applications. For example, the NPs' superparamagnetic behavior is important for their use for hyperthermia [32]; high values of magnetization and low coercivity are required to extract NPs with adsorbed pollutants from wastewater with the help of a magnetic field [22]; the distribution of magnetic ions over magnetic sublattices is important for the NPs application in catalysis [21] and so on.

The study aims to synthesize $Co_xZn_{1-x}Fe_2O_4$ NPs using the citrate precursor auto-combustion technique [31]. Citrate precursor method is a scalable technique for producing large quantity of nanoparticle and quite economic as there is no loss of materials. The goal is to trace the evolution of the distribution of Co^{2+}, Fe^{3+}, and Zn^{2+} ions over tetrahedral and octahedral positions in the crystal and the resulting magnetic properties, including magneto-optical spectra, depending on the Co content in NPs in order to expand their potential applications.

Results and discussion

Nanoparticles morphology and structure

The X-ray diffraction patterns shown in figure (Online Resource 1) revealed the spinel cubic phase of the Fd-3 m space group for all the samples. The average crystallite size of the samples calculated by Scherer's equation increases from 28 to 36 nm with increasing Co concentration in the NPs (Online Resource 2). The lattice constant decreases from 8.443 to 8.403 Å, which was associated with the smaller Co^{2+} ion radius compared to the Zn^{2+} ion radius, 0.72 and 0.74 Å, correspondingly [33].

The TEM and HRTEM analyses carried out here provided additional information on the NP morphology, local crystal structure and, especially important, elemental distribution inside the NPs. TEM images of the $Co_xZn_{1-x}Fe_2O_4$ NPs are shown in figure (Online Resource 3). NPs with irregular shapes and large size dispersions are observed for all x values. The average size of nanoparticles is 15–20% larger than the average crystallite size obtained from the analysis. This is due to the fact that electron microscopy reveals the entire particle, while XRD detects only coherent scattering regions, which are usually smaller than the particle size due to the disorder of the surface layers. As an example, the histogram of NPs size distribution

is presented in Fig. (Online Resource 4). In addition, there is a tendency for particles to combine into conglomerates. Many of the large particles seen in figure (Online Resource 3) are actually conglomerates of small particles, as can be clearly seen in the HRTEM images (Fig. 1). In Fig. 1, atomic planes are also visible even for the smallest particles; that is, they are single crystals. This explains the size of the crystallites obtained from the XRD pattern analysis. The atomic interplanar distances observed in the HRTEM images correspond to those of $ZnFe_2O_4$. According to the analysis of the SAED patterns (examples are shown in

Figs. 2(a) and 3(a)), the main phase in all the samples is $ZnFe_2O_4$ (Fd-3 m, PDF 4 + card #00-022-1012).

Figures 2 and 3 show the elemental maps for groups of NPs in samples with $x = 0.1$ and 0.4, respectively, from which a close to uniform distribution of Fe, Co, Zn, and O over the particle volume is observed. A more detailed elemental analysis of the sample with $x = 0$ indicated that it was composed of $ZnFe_2O_4$. In the samples with $x = 0.1–0.3$, Co was distributed evenly. For higher doses, when studying the local elemental composition of individual particles by the EDS method, it was found that
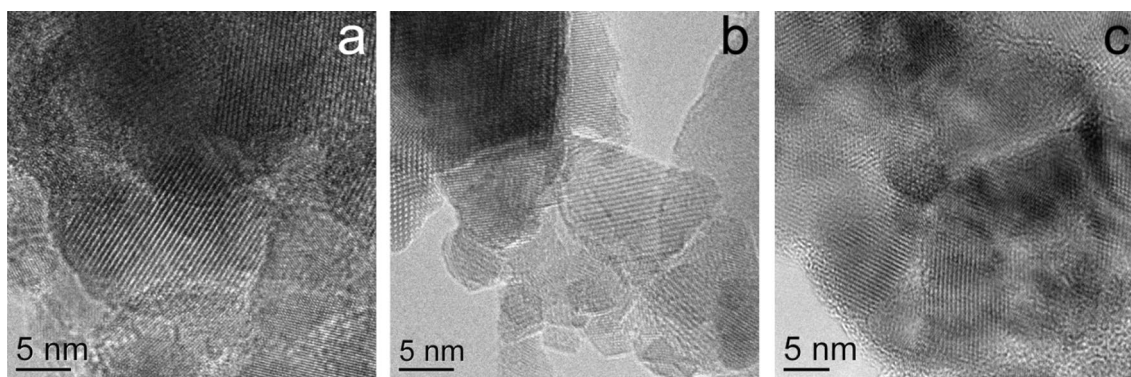

Figure 1: HRTEM images of $Co_xZn_{1-x}Fe_2O_4$ NPs for samples 1, 2, and 6 with $x = 0$, 0.1, and 0.5, panels (a–c), respectively.
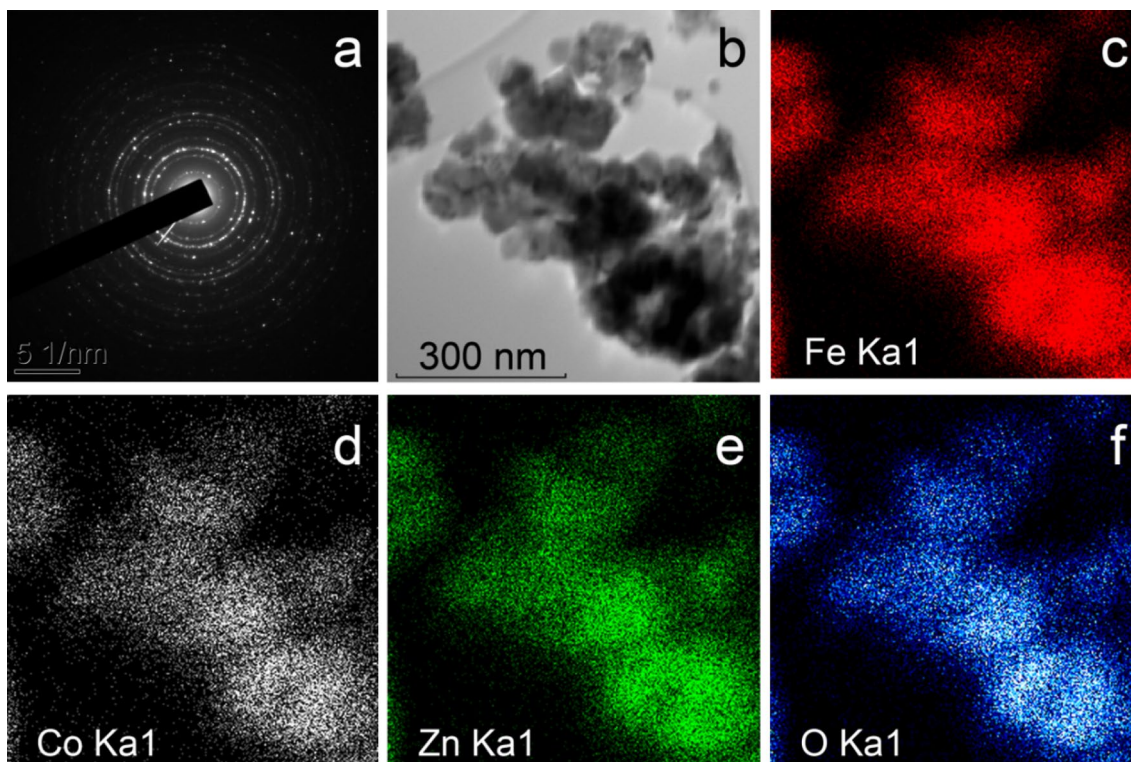

Figure 2: SAED pattern (a), TEM image (b) and corresponding EDS elemental mappings of Fe (c), Co (d), Zn (e), and O (f) for the group of NPs in the $Co_{0.1}Zn_{0.9}Fe_2O_4$ sample.
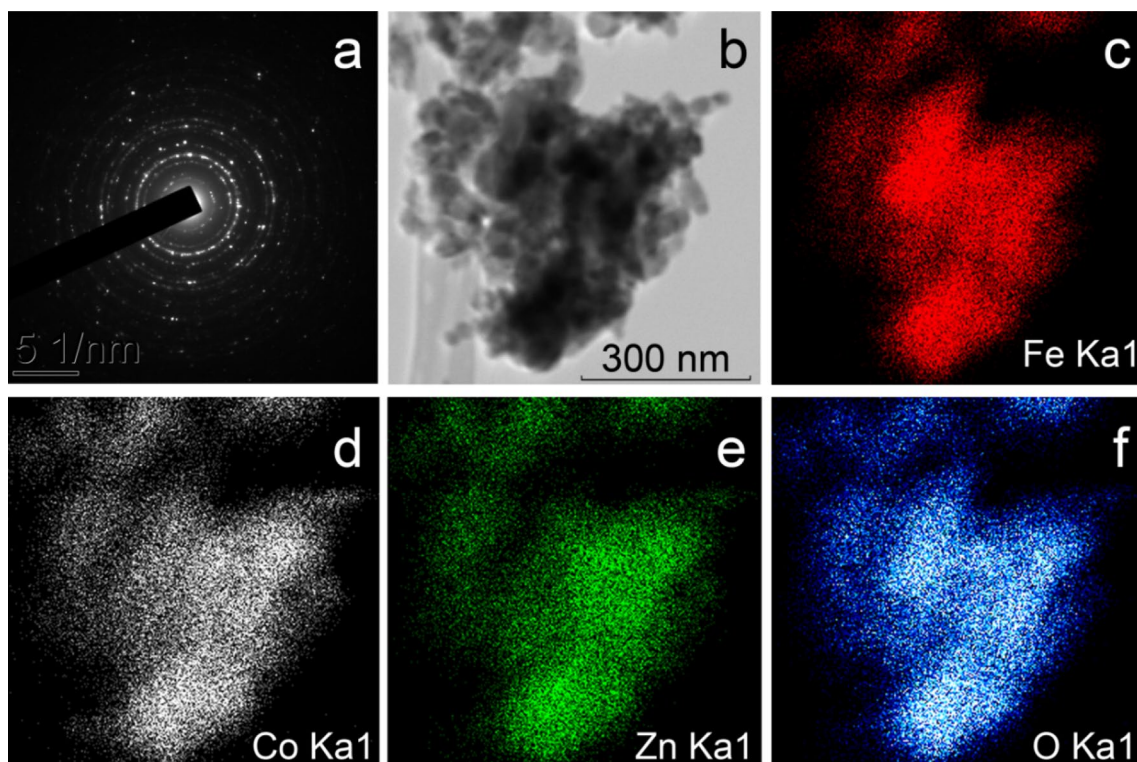
Figure 3: SAED pattern (a), TEM image (b) and corresponding EDS elemental mappings of Fe (c), Co (d), Zn (e), and O (f) for the group of NPs in the $Co_{0.4}Zn_{0.6}Fe_2O_4$ sample.

in some particles the cobalt content is somewhat lower than it should be in accordance with the given formulas. However, since neither in the XRD patterns nor in the electron diffraction pattern (Online Resource 1), diffraction reflections corresponding to phases other than $Co_xZn_{1-x}Fe_2O_4$ are observed, it can be assumed that the number of such particles is insignificant and they do not make any significant contribution to the observed properties of the samples.

Mössbauer spectroscopy

Mössbauer spectra recorded at 300 and 4.2 K are presented in Figs. 4 and 5. The characteristics of the room temperature spectra change with increasing Co concentration in a sample. The quadruple doublets dominate in the spectra of samples 1–3; sextet components are barely visible, which is evidence of the predominantly paramagnetic state of the NPs in these samples at room temperature. The relaxation characteristics of the spectra of samples 4–6 may be related to the superparamagnetic state of the NPs and proximity of the blocking temperature to the measurement temperature. Distinct sextet components appear in the spectrum of sample 6, which has the highest Co content. The observed room temperature spectra are very close to those presented in Ref. [29] for the series of $Co_xZn_{1-x}Fe_2O_4$ ($x = 0.0$,

0.1, 0.2, 0.3, 0.4, 0.5) NPs synthesized by the precursor combustion method.

Lowering the measurement temperature leads to major changes in the spectra. Well-resolved sextets characteristic of the magnetically ordered state of the NPs are observed for all samples at 4.2 K (Fig. 5); the central doublet completely disappears. These sextets can be used to estimate the ion distribution among crystal positions. The rather broad line widths of the doublets and the sextet peaks are due to the overlap of several components originating from the nonequivalent states of iron ions. Therefore, the experimental Mössbauer spectra were fitted by several sextets. The processing of the recorded spectra was performed in two stages. In the first stage, possible nonequivalent iron positions in the samples were determined by calculating the probability distributions of magnetic hyperfine fields. In accordance with the results obtained, a preliminary model spectrum was formed. In the next stage, the model spectrum was fitted to the experimental spectrum by varying the entire set of hyperfine parameters using the linear approximation of the least squares method.

The parameters of the spectra obtained as a result of their processing are shown in Table 1. The isomer chemical shift (IS) characterizes the local surroundings (octahedral or tetrahedral) of an iron ion as well as the charge state of this ion. At the same charge state, there is less IS in the tetrahedral surroundings than
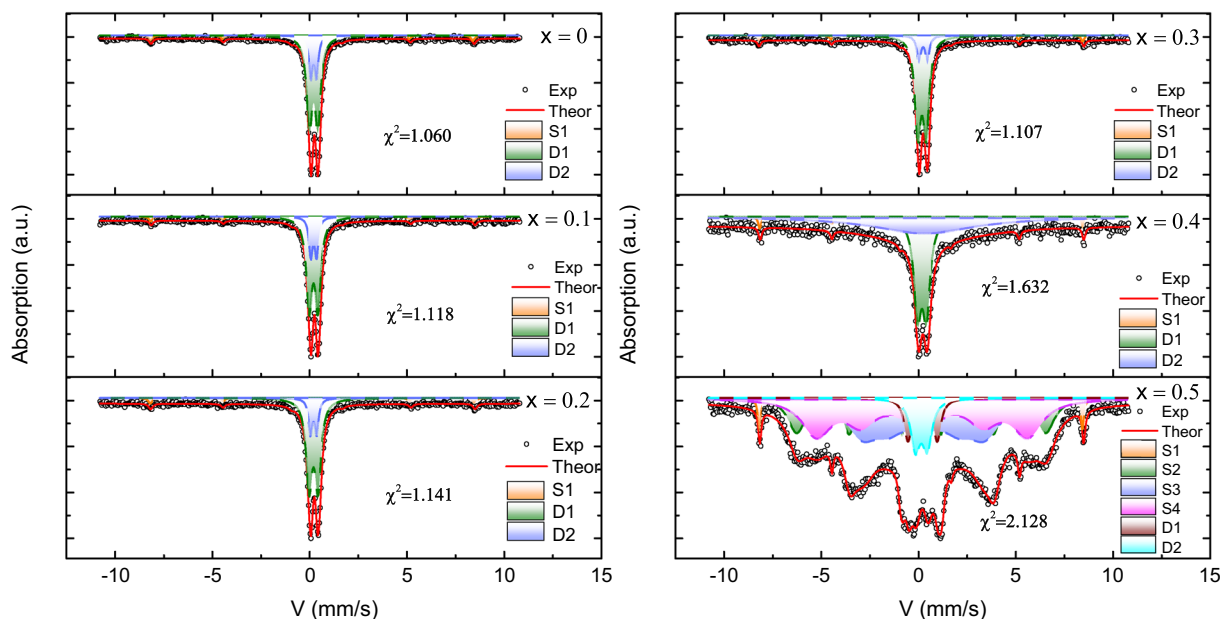
Figure 4: Mössbauer spectra of all the samples recorded at 300 K. The dots are experimental data; errors in measurements are less than the dots size. The fitted spectra are shown as red lines. Partial components are shown as colored areas. The parameter χ^2, characterizing the accuracy of experimental data processing, is specified for each sample.
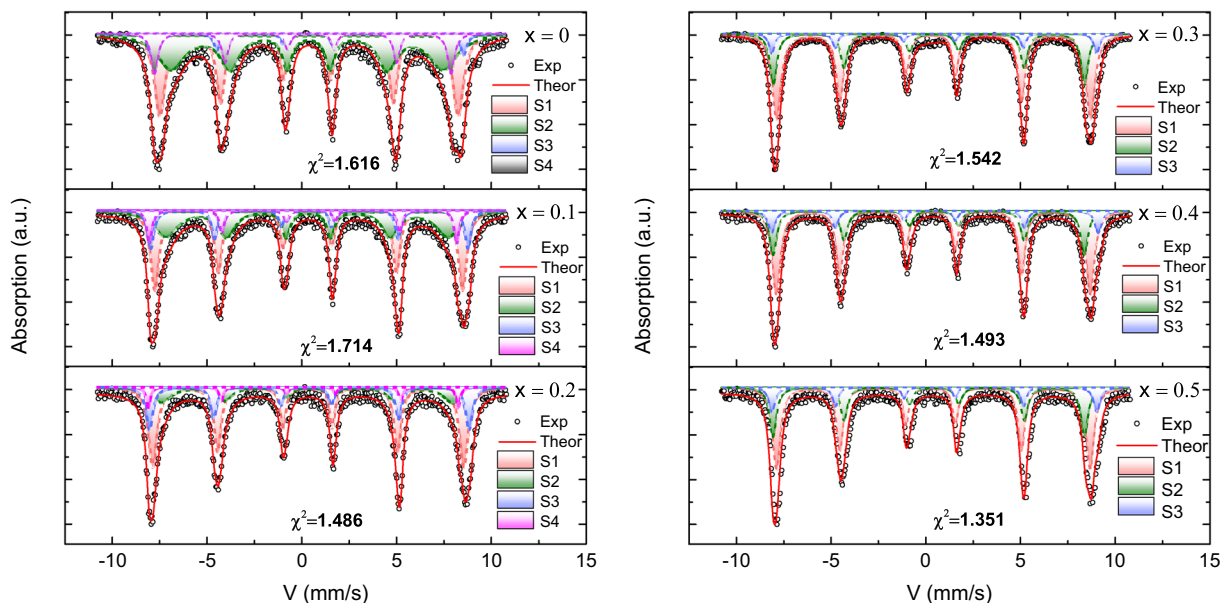

Figure 5: Mössbauer spectra of all the samples recorded at 4.2 K. The dots are experimental data; errors in measurements are less than the dots size. The fitted spectra are shown as red lines. Partial components are shown as colored areas. The parameter χ^2, characterizing the accuracy of experimental data processing, is specified for each sample.

in the octahedral surroundings because of the higher electron density on the iron nucleus. This difference allows us to distinguish the iron ion positions in the spinel lattice. However, in the case of the considered samples, such differentiation is somewhat difficult. This is due to the closeness of the temperature of the

liquid helium at which the measurements were made and the temperature of the magnetic transition in $ZnFe_2O$ ($T_N \sim 8$ K for bulk $ZnFe_2O$ [34, 35]). In addition, at room temperature, the tetra- and octahedral states are indistinguishable, which may be a consequence of the superparamagnetic state. Nevertheless,

Table 1: The parameters of the Mössbauer spectra of all samples measured at 4.2 K.

	IS, ±0.005 mm/s	H$_{hf}$ ±0.5 T	QS, ±0.02 mm/s	W, ±0.03 mm/s	dH, ±0.03 mm/s	A, ±0.03 o.e	Position
Sample 1							
1	0.476	490.9	0.214	0.363	0.323	0.39	[B]
2	0.468	447.8	− 0.145	0.399	1.371	0.43	[B]
3	0.435	514.4	0.004	0.257	0.166	0.06	[B]
4	0.412	487.6	− 0.851	0.349	0.078	0.12	(A)
Sample 2							
1	0.478	506.1	0.137	0.36	0.183	0.39	[B]
2	0.456	464.1	− 0.159	0.31	1.205	0.36	[B]
3	0.467	521.8	0.318	0.29	0.105	0.15	[B]
4	0.417	505.6	− 0.823	0.32	0	0.10	(A)
Sample 3							
1	0.471	511.6	0.065	0.32	0.22	0.51	[B]
2	0.490	478.8	− 0.257	0.51	0.668	0.21	[B]
3	0.460	525.7	0.327	0.32	0.124	0.22	[B]
4	0.424	509.9	− 0.823	0.25	0	0.06	(A)
Sample 4							
1	0.481	516.9	0.277	0.35	0.2	0.62	[B]
2	0.458	512.3	− 0.534	0.44	0	0.29	[B]
3	0.453	534.9	0.529	0.29	0.065	0.09	(A)
Sample 5							
1	0.472	517	0.271	0.35	0.176	0.60	[B]
2	0.495	512.2	− 0.566	0.46	0	0.27	[B]
3	0.440	537.6	0.539	0.28	0.15	0.13	(A)
Sample 6							
1	0.472	516.3	0.273	0.34	0.163	0.55	[B]
2	0.444	512.9	− 0.579	0.43	0	0.29	[B]
3	0.453	534.8	0.514	0.27	0.124	0.14	(A)

IS isomer chemical shift relative α-Fe, H$_{hf}$ hyperfine field on iron nuclei, *QS* quadruple splitting, *W* width of the Mössbauer line at half height, *dH* line broadening because of hyperfine field inhomogeneity, *A* relative population of positions in a crystal.

an attempt to determine whether iron belongs to the tetra- and octahedral positions can be made; however, this analysis should be performed critically. Furthermore, the obtained results are qualitatively confirmed by the magnetization measurement data, which are presented below.

According to the Mössbauer spectrum parameters presented in Table 1, the following ion distributions over the tetrahedral and octahedral positions can be proposed.

Sample 1 – $(Zn_{0.76}Fe_{0.24})$ $[Zn_{0.24}Fe_{1.76}]$ O_4.

Sample 2 – $(Zn_{0.80}Fe_{0.20})$ $[Co_{0.10}Zn_{0.10}Fe_{1.80}]$ O_4.

Sample 3 – $(Co_{0.08}Zn_{0.80}Fe_{0.12})$ $[Co_{0.12}Fe_{1.88}]$ O_4.

Sample 4 – $(Co_{0.12}Zn_{0.70}Fe_{0.18})$ $[Co_{0.18}Fe_{1.82}]$ O_4.

Sample 5 – $(Co_{0.24}Zn_{0.60}Fe_{0.26})$ $[Co_{0.26}Fe_{1.74}]$ O_4.

Sample 6 – $(Co_{0.22}Zn_{0.50}Fe_{0.28})$ $[Co_{0.28}Fe_{1.72}]$ O_4.

It can be seen that cobalt ions are distributed between tetrahedral and octahedral positions starting from $x = 0.2$, and there is an obvious tendency for the occupancy of tetrahedral positions by Co^{2+} ions to increase as the Co concentration in NPs increases. At that, all Zn^{2+} ions are concentrated only in tetrahedral positions (except sample 1) and Fe^{3+} are concentrated mainly in octahedral positions. About 10 percent of Fe^{3+} ions are localized in tetrahedral positions. Note large discrepancies between the results of various authors concerning the distribution of Co^{2+}, Zn^{2+}, and Fe^{3+} ions across the positions. For zinc ferrite NPs fabricated with the sol–gel method and with ball-mailing, the proportions of Zn^{2+} ions in the tetrahedral positions were almost the same — 0.62 and 0.58, respectively [36]. In the case of the $Co_{0.2}Zn_{0.8}Fe_2O_4$ NPs prepared via combustion, the fourth part of divalent cobalt ions is located in tetrahedral and three quarters—in octahedral positions (0.05 and 0.15, respectively) [28]. An increase in the Co concentration leads to Co^{2+} ion localization in the octahedral positions only. The system of $Co_xZn_{1-x}Fe_2O_4$ NPs with $x = 0.5$, 0.6, and 0.7 prepared by the wet-chemical co-precipitation technique was considered in Ref. [37], and the next Co^{2+} ion distribution over the crystal positions was suggested: 0.15 of the Co^{2+} ions occupy tetrahedral positions for all x, and the proportion of these ions preferring octahedral positions increases with increasing x.

Thus, one can stat that the technology used here for the synthesis of the Co–Zn-ferrite nanocrystals provides a greater presence of Co^{2+} ions in tetrahedral positions compared to the data of other authors.

Magnetic properties

The magnetization (M) curves of samples 1–6 versus applied magnetic field (H) up to 1.5 T at 300 and 100 K are presented in Fig. 6. The error in measuring magnetization (10^{-2} A m²/kg) does not exceed the width of the line in the figure. Only sample 1 with $x = 0$ demonstrates pure paramagnetic behavior at room temperature [curve 1 in Fig. 6(a)]. Even for sample 2 with $x = 0.1$, the room temperature magnetization curve deviates from the linear dependence characteristic of a paramagnetic substance [curve 2 in Fig. 6(a)], and for sample 3 with $x = 0.2$, a very narrow hysteresis loop is clearly visible [curve 3 in Fig. 6(a)]. At the same time, with an increase in the magnetic field, the magnetization of these three samples increases linearly in the field, differing significantly from the magnetization curves of samples 4–6 [Fig. 6(b, d)]. It can be assumed that some of the NPs in samples 2 and 3 are in the superparamagnetic state at room temperature, while most of the particles in those samples are paramagnetic

which is responsible for the linear increase in magnetization in high fields.

In the case of samples 4–6, the shape of the magnetization curves is typical of ferrimagnetic (or ferromagnetic) state with narrow hysteresis loops and magnetic saturation in magnetic field of about 0.3 T. A sharp magnetization increase is observed at the transition from sample 3 to sample 4, which can be interpreted as a transition from a heterogeneous magnetic state of the entire ensemble of NPs to the ferrimagnetic state of most NPs. A similar picture was observed in Ref. [22, 25, 38, 39].

As the temperature decreases to 100 K, the superparamagnetic component appears in sample 1, which does not contain Co. This follows from a change in the shape of the magnetization curve: a characteristic s-shaped bend appears near zero. An appearance of the magnetic moment in the $ZnFe_2O_4$ NPs was observed earlier (e.g., [40]), but not always. For example, magnetic ordering was not observed up to 50 K in Zn spinel NPs obtained via the co-precipitation method [11, 28]. For all other samples, upon cooling, a strong increase in the magnetization is observed. The remnant magnetization M_r and coercivity H_c also increase when cooling but to varying degrees, as shown in Table 2. All magnetic characteristics increase with increasing Co concentration in NPs approximately according to a parabolic law, as shown in Fig. 7(a) for saturation magnetization.
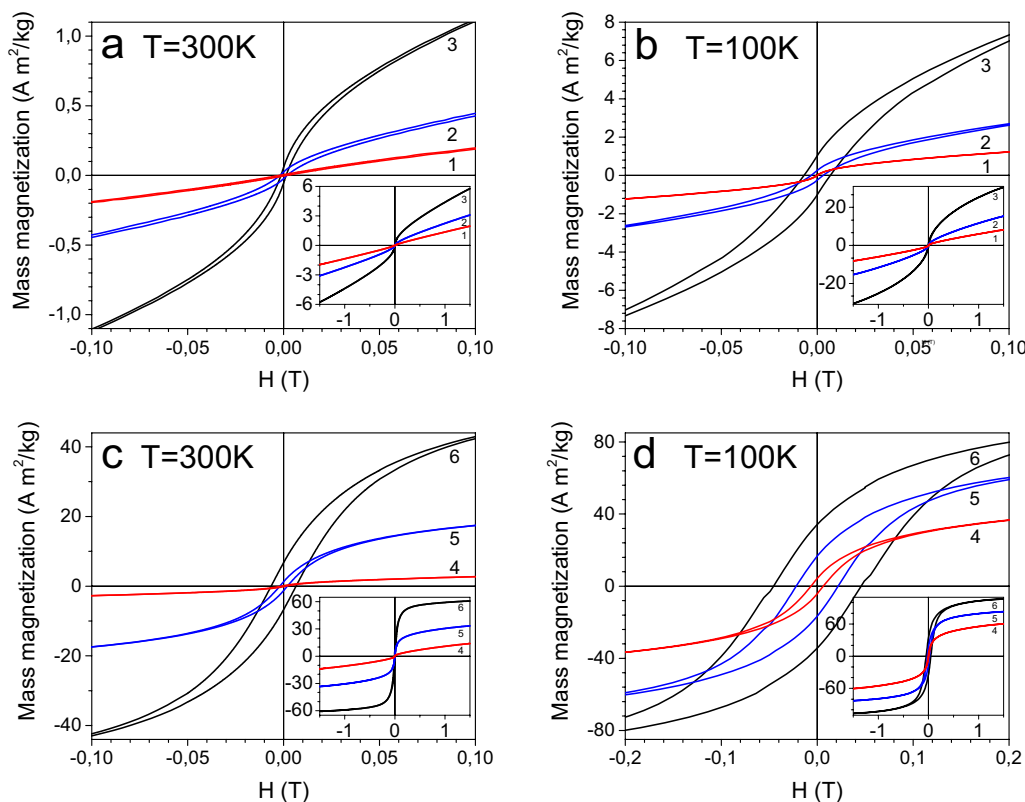

Figure 6: The field dependences of the magnetization of samples 1–6 (curves 1–6, respectively) measured at T = 300 (a, c) and 100 K (b–d). Insets: the same dependences in magnetic field up 1.5 T.

Table 2: The saturation magnetization M_s^*, coercivity H_c, and remnant M_r at 100 and 300 K.

Sample	M_s, A m^2/kg		H_c, mT		M_r, A m^2/kg	
	300 K	100 K	300 K	100 K	300 K	100 K
1	2.00	7.74	0	1.3	0	0
2	3.4	15.4	1.8	3.1	<0.1	0.2
3	5.9	30.6	1.2	6.8	<0.1	1.0
4	13.9	60.6	1.2	6.8	0.1	4.4
5	33.5	83.0	2.0	21.9	1.3	17
6	60.7	106.6	6.5	45.6	6.7	34

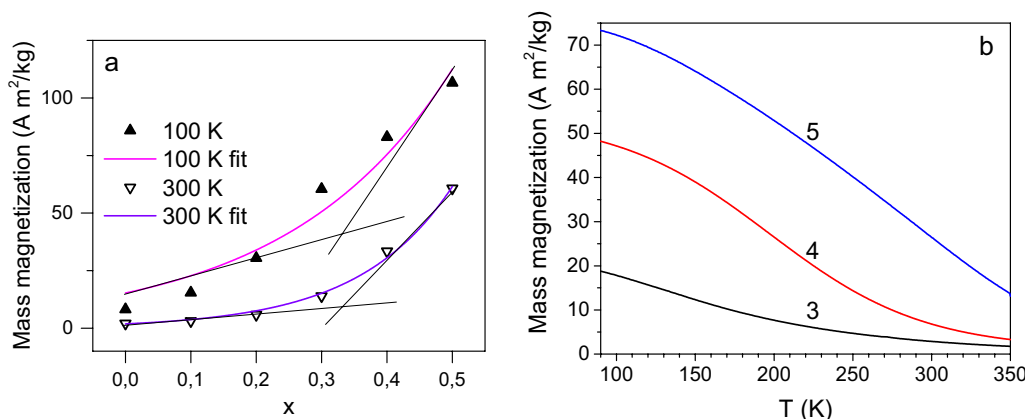*M_s was determined as M measured in a magnetic field of 1.5 T.

Figure 7: (a) Saturation magnetization concentration dependencies in the magnetic field 1.5 T at temperatures 100 and 300 K; (b) magnetization temperature dependencies of samples 3–5 with $x = 0.2$–0.4, respectively, in a magnetic field of 0.5 T.

The temperature dependences of the magnetization [Fig. 7(b)] of samples 3–5 recorded in a magnetic field of 0.5 T are similar to the FC curves for $Co_xZn_{1-x}Fe_2O_4$ NPs synthesized with the precursor combustion method shown in Ref. [29]. For the 1 and 2 samples, magnetization temperature dependences are similar to that for sample 3 but with smaller increase when the temperature approaches to 100 K. Several mechanisms are responsible for the increase in the magnetization of NPs with decreasing temperature. The increase in the magnetic moment of each NP obeys the Curie law for paramagnets or the Langevin law for magnetically ordered media, as does the alignment of magnetic moments in the direction of the applied magnetic field. The shape of the temperature dependence curves confirms the conclusion made during the interpretation of the magnetization curves about the concentration transition from the predominantly paramagnetic to the ferrimagnetic state of NPs between Co concentrations of $x = 0.2$ and $x = 0.3$.

Magnetic circular dichroism

It seems reasonable to consider studies of the magneto-optical properties of cobalt ferrite compounds available in the literature before presenting the results of the MCD study. Several authors have devoted their efforts to studying the magneto-optics of the stoichiometric cobalt ferrite $CoFe_2O_4$. Basically, these were studies of the spectral dependences of the Kerr effect (KE) in the reflected light, calculations of the off-diagonal components of the dielectric tensor, and attempts to understand the origin of the electron transitions responsible for the effect [41–50]. The authors of [51] revealed a rather high Kerr effect in nanocrystalline $ZnFe_2O_4$ films. The magneto-optics of cobalt ferrite when its composition deviates from stoichiometry or when cobalt ions are replaced by other ions have been considered in a few works. The Kerr effect in single crystals of the $CoFe_{2-x}Co_xO_4$ system was investigated in Ref. [52], in bulk $CoFe_{2-x}Ga_xO_4$ ferrite in Ref. [53], and in nanocrystalline $CoFe_{2-x}M_xO_4$ (M = Mn, Al, Sc) thin films in Ref. [54]. MCD in transmitted light was investigated in Ref. [55] for the high-quality epitaxial $CoFe_2O_4$ films (30–200 nm) grown on (001)-orientated $MgAl_2O_4$ single crystal. MCD in the transmitted light was investigated in $CoFe_2O_4$ NPs synthesized by the co-precipitation method [56]. Spectra of the components of the dielectric tensor ε calculated based on the measured Faraday rotation and ellipticity were presented in Ref. [57] for the epitaxial $Co_xFe_{3-x}O_4$ (001) thin films fabricated with magnetron sputtering. At that, the spectrum of the imaginary part of the off-diagonal component ε" was similar in shape to the

MCD spectrum of the epitaxial $CoFe_2O_4$ film [55]. In Ref. [58], MCD spectral dependences were studied for the $Zn_{1-x}Co_xFe_2O_4$ ($0 \leq x \leq 1$) (111) composition-spread thin film epitaxially grown on a $MgAl_2O_4$ (111) substrate by combinatorial pulsed laser deposition. Sequential deposition of the two end-compounds with monolayer-period led to the formation of solid solution with addressable composition, which led to the appearance of MCD spectra significantly different from the spectra of homogeneous Co-ferrite samples.

The MCD spectra of the investigated $Co_xZn_{1-x}Fe_2O_4$ NPs are shown in Fig. 8. For better readability, Fig. 8(c, d) show smoothed data. The error was determined by the sensitivity of the photomultiplier tube and is indicated by the error bars. In

Fig. 8(c, d), the bars are shown for one curve to avoid cluttering the graph. In Fig. 8(e, f), the error does not exceed the line width. For samples 1 and 2, the room temperature MCD signal is at the noise level. However, upon cooling to 100 K, in the first case, one can note the appearance of a broad structure with a positive sign in the region of 2.5–3.5 eV, and in the second case, negative peaks near 1.7 and 2.2 eV. A clear picture is observed starting with $x = 0.2$ [Fig. 8(c)].

With a further increase in x, the shape of the spectra in the region of 1.2–2.2 eV does not change, and only the intensity of the band increases [Fig. 8(d–f)]. In the higher energy region, the broad structured band observed for the sample with $x = 0.2$ is modified into an asymmetric maximum centered at 2.5 eV.
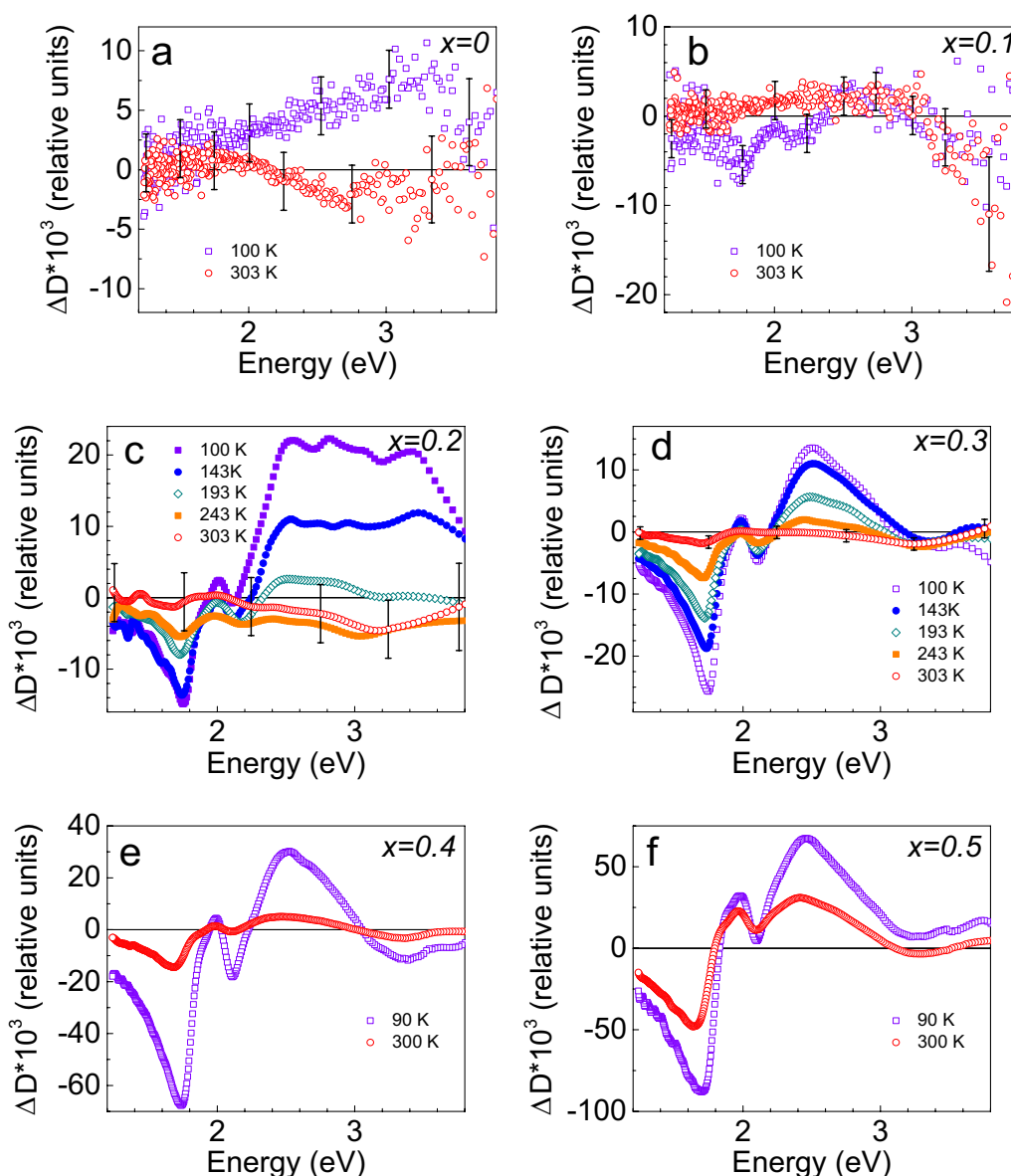

Figure 8: The MCD spectra of $Co_xZn_{1-x}Fe_2O_4$ NPs at different temperatures. The Co concentration (x) is shown in each panel.

This shape of the spectrum is also preserved for samples 5 and 6 with $x = 0.4$ and 0.5. The situation looks as if the MCD spectral dependence in the samples is associated mainly with cobalt ions. It is worth comparing the spectra recorded at 300 K with the MCD spectra for thin $Co_xZn_{1-x}Fe_2O_4$ films given in Ref. [58] recorded also at 300 K. One can note the close similarity of the shape of the spectra in the region 1.8–3.0 eV: the wide band consisting of at least two overlapping peaks. In our case, this band shifts a little bit to higher energies comparing to that in Ref. [58]. In addition, the peaks in our case are better resolved. At higher light wave energies, the picture is not so clear because, due to the stronger light absorption by the silicone matrix, we were unable to measure the MCD at energies above 4.1 eV. However, an increase in the MCD signal is visible starting from 3.55 eV with a characteristic inflection near 3.7 eV.

Let us now pay attention to the intense, relatively narrow peak at 1.75 eV, which becomes visible already in the spectrum of sample 2 with $x = 0.1$. In the case of thin films [58], this peak was not observed, perhaps it remained outside the observation area since the entire spectrum is slightly shifted to lower energy values comparing to our case. Meanwhile, the wavelength corresponding to the center of gravity of this peak matches exactly to the emission wavelength (710 nm) of some lasers, e.g., ALP-710 nm, manufactured by NKT Photonics (Denmark), and light emitting diodes manufactured by many companies in the world, for example, by BMI SURPLUS Inc. (USA), which may be of interest for photonic devices.

Spectra recorded at lower temperatures are much better resolved and therefore are more informative. For example, a signal at the noise level is recorded at 300 K for sample 3 with $x = 0.2$. When cooled to 193 K, a spectrum with a number of features appears and develops further with decreasing temperature. A similar picture is observed for sample 4 with $x = 0.3$. In this case, the spectrum at energies less than 2.3 eV is similar to the spectrum of sample 3, but at higher energies of the light wave, it changes significantly and remains the same with a further increase in x.

The MCD spectra shown in Fig. 8 can be compared with the spectra of the polar Kerr effect (PKE) or the transverse Kerr effect (TKE) given in a number of works. The comparison of the PKE, TKE, and MCD spectra seems to be quite natural because all the effects, MCD (θ_F), PKE (θ_{Kp}), and TKE (θ_{Kt}), are described by similar equations [39, 59]:

$$\theta_F = \frac{4\pi}{\lambda}\left\{\frac{n}{k^2 + n^2}\varepsilon_{xy}'' - \frac{k}{k^2 + n^2}\varepsilon_{xy}'\right\}, \quad (1)$$

$$\theta_{K_p} = \frac{B}{B^2 - A^2}\varepsilon_{xy}'' - \frac{A}{B^2 - A^2}\varepsilon_{xy}', \quad (2)$$

$$\theta_{K_t} = a(n, k, \varphi)\varepsilon_{xy}' + b(n, k, \varphi)\varepsilon_{xy}'', \quad (3)$$

where ε_{xy}' and ε_{xy}'' are the real and imaginary parts of the off-diagonal component of the dielectric tensor ε; n and k are the refractive index and absorption coefficient, respectively; λ is the light wavelength; and A, B, a, and b are functions of n, k, and φ (in the case of TKE).

Sample 1 contains only one type of magnetic ion, Fe^{3+}. In the bulk $ZnFe_2O_4$ spinel, these ions occupy octahedral positions, and the superexchange interaction between them provides antiferromagnetic ordering at T < 10 K, as mentioned in the introduction. In small magnetic particles, no equilibrium states can arise, and redistribution of Fe^{3+} ions between sublattices can occur, leading to magnetic ordering [37], which is what occurs in our case, according to the VSM data (Fig. 6). Since there are no other magnetic ions in this sample except Fe^{3+}, one can compare the MCD spectrum with the TKE spectra of the $MgFe_2O_4$ polycrystalline sample and single-crystal film and the $LiFe_2O_4$ single crystal [42]. TKE spectra in all these cases coincide with each other. They contain four peaks in the region of 2–4 eV: one very weak at 2.3 eV and three overlapping peaks at 2.6, 3.25, and 3.9 eV. Authors of Ref. [42] ascribed them to the single-ion transition $^6A_{1g}(^6S)$–$4E_g(^4G)$ and two-exciton transitions $2T_{1g}$, $T_{1g} + T_{2g}$, and $2T_{2g}$, respectively, where the energies of T_{1g} and T_{2g} were 1.3 and 1.95 eV, respectively. These types of transitions can mainly contribute to the wide positive structure in the MCD spectra of the sample 1 with $x = 0.0$ [Fig. 8(a)]. In samples 3–6, Co^{2+} ions partially occupy tetrahedral positions instead of nonmagnetic Zn^{2+} ions, as follows from Mössbauer data, and thereby contribute to an increase in intersublattice indirect exchange interactions. At that, two variants are possible. (i) The Fe^{3+} ions move from octahedral to tetrahedral positions due to cobalt's preference for the octahedral positions, which leads to an increase in the MCD signal due to the excitation of Fe^{3+} ions at energies higher than 2.2 eV [Fig. 8(c)]. (ii) Despite the cation distribution in a single crystal corresponding to the formula $[Fe^{3+}](Co^{2+}Fe^{3+})O_4$ [60], deviations from such a distribution were observed by several authors (e.g., [61]) in nanostructured samples and thin films depending on the synthesis conditions, and cobalt ions can partially enter tetrahedral positions in accordance with the formula $\left[Co_\delta^{2+}Fe_{1-\delta}^{3+}\right]\left(Co_{1-\delta}^{2+}Fe_{1+\delta}^{3+}\right)O_4$. The ratio between the Fe^{3+} and Co^{2+} content in tetrahedral positions can vary depending on the technological conditions.

Along with the features caused by electronic transitions associated with the Fe^{3+} ions, a negative peak at 1.75 eV appears in the MCD spectrum at the minimal Co addition [Fig. 8(b)], which is characteristic of the $CoFe_2O_4$ crystals [62] and films as well for Ga-diluted $CoFe_2O_4$ NPs [53]. The MCD spectra of the samples with $x \geq 0.3$ are close in shape to the PKE spectrum of the $CoFe_2O_4$ thin film prepared with sol–gel techniques. Spectrum was characterized by extrema centered near 1.8, 2.2, 2.6, and 3.5 eV [48]. A similar PKE spectrum (shifted along the

y-axis) was observed for the $CoFe_2O_4$ epitaxial thin film grown on Nb-doped $SrTiO_3(100)$ substrates by pulsed laser deposition [49]. The appearance of the MCD spectrum typical for cobalt ferrite in samples 4–6 allows one to conclude that the long-range magnetic order in these samples is established upon going from $x = 0.2$ to $x = 0.3$, which is consistent with the VSM data.

The nature of the magneto-optical spectra of ferrites is still a subject of discussion despite the rather long history of their research [63]. Several electronic processes are considered to explain the features of the ferrite magneto-optical spectra. Among them, there are (i) the electron transition between cations of different valences (intervalence charge transfer—IVCT), (ii) the electron transition between cations of different sublattices (intersublattice charge transfer—ISCT), (iii) the single-ion transition between the ion ground and excited states split by the crystal field (CF), so-called CF transitions, (iv) the exciton–magnon transitions when two neighboring ions coupled by exchange interactions are simultaneously excited, and (v) the transition from the O_{2p} band to the electronically higher cation band. For cobalt ferrite, the results of the Kerr effect spectra investigation and their analysis presented by different authors were somewhat different. This can be attributed to the very strong dependence of the measured KE on the sample surface quality and on the difference in the cation Co^{2+} and Fe^{3+} distributions between the octahedral and tetrahedral positions in the surface layers of samples. Nevertheless, most authors who studied the KE spectra of cobalt ferrite observed features in KE spectra or in the ε''_{xy} spectra near energies of 1.8 and 2.2 eV, which were identified as the CF spin-allowed transition in the tetrahedral-coordinated Co^{2+} ion $^4A_2 \rightarrow {}^4T_2(t_2^5e^2)$ and IVCT $[Co^{2+}]$ $t_{2g} \rightarrow [Fe^{3+}]t_{2g}$, respectively [42, 43, 46, 52, 62, 64, 65]. Similarly, features in the MCD spectrum of cobalt ferrite NPs at energies of 1.81 and 2.25 eV were identified in Ref. [55]. It should be noted here that the CF transitions in Co^{2+} ions with the $3d^7$ electronic configuration occur at close values of the light wave energy in both tetrahedral and octahedral coordination [66]. To compare the bands in the optical absorption spectrum of 3d ions with d-d electronic transitions, the spectra of impurity ions are usually studied in crystals where they occupy only one type of portions. For example, optical spectra of Co^{2+} ions in ZnO, ZnS, and CdS crystals, where they are localized in tetrahedral positions only, and in MgO single crystal, where they occupy octahedral positions, were studied in detail in Ref. [67, 68], correspondingly. In both cases, the spectra contained a set of absorption bands located at close values of the light wave energy. In particular, an absorption band centered at 1.7 eV was present in the absorption spectrum of MgO crystal with embedded Co^{2+} ions. Thus, the correlation of the observed negative MCD peak in the region of 1.7–1.8 eV with the transition in tetrahedral-coordinated Co^{2+} ions seems ambiguous. Detection of such an MCD peak in a sample with $x = 0.1$ [Fig. 8(b)] containing ions

only in octahedral positions, according to the Mössbauer effect data, allows us to associate it with the spin-allowed transition in the Co^{2+} ions in octahedral positions. The peak positions in the KE or MCD spectra at higher light wave energies and their identification are different among different authors too. For example, Zviagin and coauthors [64] referred to the feature at 2.64 eV for ISCT $(Fe^{3+})t_2 \rightarrow [Fe^{3+}]t_{2g}$ and the feature at 3.41 eV for IVCT $[Co^{2+}]t_{2g} \rightarrow [Fe^{3+}]e_g$. Fontijn and coworkers [46] analyzing the experimental results presented in Ref. [52, 62] reported that the extremum in the ε''_{xy} spectrum of $CoFe_2O_4$ observed at 2.6 eV was the same as that observed in Ref. [64], but the feature near 3.55 eV was associated with ISCT $[Fe^{3+}]e_g \rightarrow (Fe^{3+})t_2$. Gromova and coauthors [55] observed no peaks in the interval between 2.25 and 2.92 eV and ascribed the peaks revealed at higher energies to the CF transitions in Fe^{3+} ions. Krinchik and coauthors [42, 43] considered features in the TKE spectra at higher energies as originating from the pair transitions. Thus, the origin of the magneto-optical spectra of ferrites, particularly cobalt ferrite, is rather complicated. A more detailed study of MCD in dilute cobalt ferrites is currently in progress.

Conclusion

The $Co_xZn_{1-x}Fe_2O_4$ NPs with x varying from 0.0 to 0.5 were successfully synthesized by the citrate precursor auto-combustion method, which is a scalable technique for producing large quantity of nanoparticle and quite economic as there is no loss of materials. According to the XRD patterns, as well as the interplanar spacing well resolved in the HRTEM images, the NPs were nanocrystals of the $ZnFe_2O_4$ (Fd-3 m) structure. The distribution of Co^{2+}, Fe^{3+}, and Zn^{2+} ions over tetrahedral and octahedral positions in the crystal has been established, which plays a key role in the formation of the magnetic properties of NPs. Unlike NPs of similar composition synthesized by other methods, in the case under consideration, the Fe^{3+} ions occupy preferably octahedral positions at all Co concentrations used: the amount of iron in tetrahedral positions was about ten percents, first decreasing from 12% at $x = 0.0$, passing through a minimum at $x = 0.2$ (8%), and increasing again to 14% at $x = 0.5$. The fraction of Co ions occupying tetrahedral positions also changes somewhat with changes in their concentration: Co was included only in octahedral positions at $x = 0.1$. The ratio of the Co^{2+} ions amount in tetrahedral and octahedral positions tends to 1:1 as the Co concentration in NPs increases.

Purely paramagnetic behavior at room temperature was observed only for the sample with $x = 0.0$. For all other compositions, already at room temperature, field dependences of magnetization characteristic of a magnetically ordered state were observed. For the composition with $x = 0$ at 100 K, a nonlinear dependence of magnetization on the external magnetic field also arose. The saturation magnetization increased with increasing

x, first slowly ($x = 0.1$–0.3) and then very quickly ($x = 0.4$, 0.5) approximately according to the parabolic law. For $x = 0.5$, the saturation magnetization reached the value 60 A m^2/kg which is very close to that of bulk Co-ferrite (66.3 A m^2/kg) where Co content is 1.0. Combination of high magnetization with very low coercivity (6 mT for $x = 0.5$ at T = 300 K) makes the NPs rather attractive for applications.

The MCD spectra of NPs were shown to change strongly with the Co concentration increase. For pure Zn-ferrite NPs ($x = 0$), a clearly visible but noisy MCD signal was detected, indicating the formation of a magnetically ordered phase in accordance with the magnetic data and low-temperature Mössbauer spectrum. An increase in the MCD signal and pronounced changes in the MCD spectra were observed with increasing Co concentration in the NPs. Analysis revealed that octahedral coordinated Co^{2+} ions contributed greatly to the low-energy part of the MCD spectra. Particular attention was paid to the MCD peak centered at 1.75 eV. The wavelength corresponding to the center of gravity of this peak matches exactly to the emission wavelength (710 nm) of some lasers, e.g., ALP-710 nm, manufactured by NKT Photonics (Denmark), and light emitting diodes manufactured by many companies in the world, for example, by BMI SURPLUS Inc. (USA). This made the investigated NPs to be of interest for photonic devices. Investigations in this direction are in progress now.

Methods and experimental details

Synthesis

Co$_x$Zn$_{1-x}$Fe$_2$O$_4$ NPs with $x = 0$, 0.1, 0.2, 0.3, 0.4, and 0.5 and samples 1–6 were prepared by using the citrate precursor technique as described in Ref. [31]. Stoichiometric amounts of analytical-grade materials, zinc nitrate hexahydrate (Zn(NO$_3$)$_2$·6H$_2$O, Sigma—Aldrich; 98% purity), cobalt nitrate hexahydrate (Co(NO$_3$)$_2$·6H$_2$O, Sigma—Aldrich; 99% purity), and iron(III) nitrate nonahydrate (Fe(NO$_3$)$_3$·9H$_2$O, Sigma—Aldrich 98% purity) were first dissolved in a beaker containing 125 mL of distilled water. Five grams of citric acid was added to the solution containing metal nitrates and then stirred at 80 °C to obtain a homogeneous solid solution. Thereafter, the samples were presintered at 700 °C for 3 h in a muffle furnace, followed by cooling to room temperature.

Methods

The crystal structure of the NPs was studied with a Japanese X-ray diffractometer (Rigaku Minifiex 600) using CuKα radiation ($\lambda = 1.5405$ Å). The 2θ values varied in the range from 20° to 90° with a step size of 0.02°. The morphology, microstructure, and local elemental composition of the NPs were investigated via high-resolution transmission electron microscopy (HRTEM)

using a JEM-2100 (JEOL Ltd.) microscope operating at an accelerating voltage of 200 kV. The microscope was equipped with an energy dispersive spectrometer (EDS), Oxford Instruments, which was used to control the elemental composition of individual NPs.

The Mössbauer spectra of the samples were recorded on an MS-1104Em spectrometer (made by the Research Institute of Physics of Southern Federal University, Rostov, Russia) in transmission geometry with a Co^{57} (Rh) radioactive source at different temperatures.

The dependence of the magnetization on an external magnetic field and temperature was studied with a vibrating sample magnetometer (VSM) (Lake Shore 8604) in a magnetic field up to 1.5 T at temperatures ranging from 90 to 350 K. The magnetic moment measurements were carried out with an accuracy of at least 10^{-7} A m^2, and the sample mass was $\sim 10^{-2}$ g (with a measurement accuracy of 10^{-5} g).

The MCD was measured using specially prepared samples: transparent plane-parallel plates made of a mixture of NP powder with silicon-based glue ("Rayher" art. no. 3338100) with a weight proportion of 0.5/100. The plates were placed in the laboratory-made measuring device so that their plane was normal to the direction of propagation of the light beam and external magnetic field. The MCD was measured as the difference in optical density ($\Delta D = D+ - D-$) of the samples for light waves right (D+) and left (D−) circularly polarized relative to the direction of sample magnetization in the spectral range of 1.2–3.8 eV in a magnetic field up to 1.3 T at temperatures of 80–300 K. The measurement accuracy was approximately 10^{-4}, and the spectral resolution was 20–50 cm^{-1} depending on the wavelength.

Author contributions

Conceptualization: Atul Thakur, Irina Edelman, and Sergey Ovchinnikov; supervision: Atul Thakur and Irina Edelman; writing—review & editing: Atul Thakur and Sergey Ovchinnikov; writing—original draft: Irina Edelman; Methodology: Dmitry Petrov; Investigation: Dmitry Petrov (magnetic circular dichroism), Sergey Zharkov (transmission electron microscopy), Yuri Knyazev (Mössbauer effect), and Aleksander Sukhachev (magnetization); Visualization, Project administration, and Data curation: Preeti Thakur; Validation: Sergey Zharkov.

Data availability

The data used to support the finding of this study are included with in the article.

Code availability

No codes were generated or analyzed during the current study.

Declarations

Conflict of interest On behalf of all authors, the corresponding author states that there is no conflict of interest.

Ethical approval

Not applicable.

Consent to participate

Not applicable.

Consent for publication

Not applicable.

Supplementary Information

The online version contains supplementary material available at https://doi.org/10.1557/s43578-024-01442-1.

References

1. K. Chandramouli, B. Suryanarayana, P.P. Varma, V. Raghavendra, K.A. Emmanuel, P. Taddesse, N. Murali, T.W. Mammo, D. Parajuli, Effect of Cr3+ substitution on dc electrical resistivity and magnetic properties of Cu0.7Co0.3Fe2−xCrxO4 ferrite nanoparticles prepared by sol-gel auto combustion method. Results Phys. **24**, 104117 (2021). https://doi.org/10.1016/j.rinp.2021.104117

2. H.R. Daruvuri, N. Murali, M. Madhu, A. Ramakrishna, D. Parajuli, M.P. Dasari, Effects of Zn2+ substitution on the structural, morphological, DC electrical resistivity, permeability and magnetic properties of Co0.5Cu0.5-xZnxFe2O4 nanoferrite. App. Phys. A (2022). https://doi.org/10.1007/s00339-022-06298-y

3. D. Parajuli, P. Taddesse, N. Murali, K. Samatha, Correlation between the structural, magnetic, and dc resistivity properties of Co0.5M0.5-xCuxFe2O4 (M = Mg, and Zn) nano ferrites. Appl. Phys. A **128**, 58 (2022). https://doi.org/10.1007/s00339-021-05211-3

4. H.R. Daruvuri, K. Chandu, N. Murali, D. Parajuli, M.P. Dasari, Effect on structural, dc electrical resistivity, and magnetic properties by the substitution of Zn2+ on Co–Cu nano ferrite. Inorganic Chem. Commun. **143**, 109794 (2022). https://doi.org/10.1016/j.inoche.2022.109794

5. R. Thakur, F. Verma, B. Wan, I. Ravelo, S. Edelman, P. Ovchinnikov, Thakur, Investigation of structural, elastic and magnetic properties of Cu2+ ions substituted cobalt nano ferrites. J. Magn. Magn. Mater. **581**, 170980 (2023). https://doi.org/10.1016/j.jmmm.2023.170980

6. D. Hamad, N. Afify, M. Omer, G. Abbady, Structure and magnetic properties of Cd(1−x)CoxFe2O4 stoichiometric nanoferrite system. Ceram. Inter. **49**, 13924–13932 (2023). https://doi.org/10.1016/j.ceramint.2022.12.274

7. K.L.V. Nagasree, B. Suryanarayana, V. Raghavendra, A. Penta, N. Murali, K. Samatha, Cu–Ce substituted cobalt nano ferrite—Structural, morphological, and magnetic behavior prepared by sol-gel auto-combustion. J. Indian Chem. Soc. **100**(7), 101025 (2023). https://doi.org/10.1016/j.jics.2023.101025

8. J.K. Babu, S. Erfan, N. Revathi, K. Vagdevi, G.S. Reddy, M.V.N.V. Sharma, Enhanced magnetic properties of Co0.5Cu0.25Zn0.25Fe2-xCrxO4 nano ferrites. J. Mater. Sci. Mater. Electron. **35**, 1441 (2024). https://doi.org/10.1007/s10854-024-13217-9

9. V.S. Rao, V. Prasad, A.R. Rao, K.A. Kumar, T.M. Mohan, Effect of Zn2+ substitution on DC electrical resistivity and magnetic properties of Mg0.5−xZnxCo0.5Fe2O4 nano ferrite. J. Mater. Sci. Mater. Electron. **35**, 1398 (2024). https://doi.org/10.1007/s10854-024-13166-3

10. M.A. Mousa, A.M. Summan, M.A. Ahmed, A.M. Badawy, Electrical conduction in γ-irradiated and unirradiated Fe3O4, CdFe2O4 and CoxZnl-xFe2O4 (0≤x≤1) ferrites. J. Mater. Sci. **24**, 2478–2482 (1989). https://doi.org/10.1007/BF01174515

11. T. Slatineanu, A.R. Iordan, V. Oancea, M.N. Palamaru, I. Dumitru, C.P. Constantin, O.F. Caltun, Magnetic and dielectric properties of Co–Zn ferrite. Mater. Sci. Eng. B **178**, 1040–1047 (2013). https://doi.org/10.1016/j.mseb.2013.06.014

12. .J.Smit, H.P. Wijn, Ferrites. Physical properties of ferrimagnetic oxides in relation to their technical applications. (Philips' Techn Libr, Eindhoven, 1959). https://archive.org/details/ferritesphysical0000smit/page/n5/mode/2up

13. P.A. Vinosha, A. Manikandan, A.S.J. Ceicilia, A. Dinesh, G.F. Nirmala, A.C. Preetha, Y. Slimani, M.A. Almessiered, A. Baykal, B. Xavier, Review on recent advances of zinc substituted cobalt ferrite nanoparticles: synthesis characterization and diverse applications. Ceram. Inter. **47**, 10512–10535 (2021). https://doi.org/10.1016/j.ceramint.2020.12.289

14. P.A. Rao, K.S. Rao, T.R.K.P. Raju, G. Kapusetti, M. Choppadandi, M.C. Varma, K.H. Rao, A systematic study of cobalt-zinc ferrite nanoparticles for self-regulated magnetic hyperthermia. J. Alloys Compd.oys Compd. **794**, 60–67 (2019). https://doi.org/10.1016/j.jallcom.2019.04.242

15. A.S. Kamzin, I.M. Obaidat, V.G. Semenov, V. Narayanaswamy, I.A. Al-Omari, B. Issa, I.V. Buryanenko, Development and characterization of magnetric nanoparticles Co1−xZnxFe2O4 (0≤x≤0.6) for biomedical applications. Phys. Sol. St. **65**, 482–496 (2023). https://doi.org/10.21883/FTT.2023.03.54749.544

16. A.V. Motorzhina, V.K. Belyaev, V.G. Kolesnikova, S. Jovanovic, L.V. Panina, K.V. Levada, Zinc-doped gold/cobalt ferrite nanoparticles in studying the cytotoxic effect on t-lymphoblastic leukemia cells. Nanobiotechnol. Rep. **17**, 436–443 (2022). https://doi.org/10.1134/S2635167622030120

17. P. Veverka, L. Kubíčková, Z. Jirak, V. Herynek, M. Veverka, O. Kaman, Temperature and field dependences of transverse relaxivity of Co–Zn ferrite nanoparticles coated with silica: The role of magnetic properties and different regimes. Mater. Chem. Phys. **260**, 124178 (2021). https://doi.org/10.1016/j.matchemphys.2020.124178

18. Y.S. Haiduk, E.V. Korobko, K.A. Shevtsova, D.A. Kotsikau, I.A. Svito, A.E. Usenka, D. Ivashenkoa, A. Fakhmi, V.V. Pankov, Synthesis, structure and magnetic properties of cobalt-zinc nanoferrite for magnetorheological liquids. Cond. Mat. Interph. **22**, 28–38 (2020). https://doi.org/10.17308/kcmf.2020.22/2526

19. A. Omelyanchik, K. Levada, S. Pshenichnikov, M. Abdolrahim, M. Baricic, A. Kapitunova, A. Galieva, S. Sukhikh, L. Astakhova, S. Antipov, B. Fabiano, D. Peddis, V. Rodionova, Green synthesis of Co–Zn spinel ferrite nanoparticles: magnetic and intrinsic antimicrobial properties. Materials **13**, 5014 (2020). https://doi.org/10.3390/ma13215014

20. O.K. Mmelesi, N. Masunga, A. Kuvarega, T.T. Nkambule, B.B. Mamba, K.K. Kefeni, Cobalt ferrite nanoparticles and nanocomposites: Photocatalytic, antimicrobial activity and toxicity in water treatment. Mater. Sci. Semicond. Process. **123**, 105523 (2021). https://doi.org/10.1016/j.mssp.2020.105523

21. T. Tsoncheva, R. Ivanova, N. Velinov, D. Kovacheva, I. Spassova, D. Karashanova, N. Petrov, Design and catalytic behavior of hosted in activated carbon foam CoxZn1-xFe2O4. Symmetry **13**, 1532 (2021). https://doi.org/10.3390/sym13081532

22. R. Sagayaraj, S. Aravazhi, G. Chandrasekaran, Review on structural and magnetic properties of (Co–Zn) ferrite nanoparticles. Int. Nano. Lett. **11**, 307–319 (2021). https://doi.org/10.1007/s40089-021-00343-z

23. G. Márquez, V. Sagredo, R. Guillén-Guillén, G. Attolini, F. Bolzoni, Calcination effects on the crystal structure and magnetic properties of CoFe2O4 nanopowders synthesized by the coprecipitation method. Revista Mexicana de Física **66**, 251–257 (2020). https://doi.org/10.31349/RevMexFis.66.251

24. T.A.S. Ferreira, J.C. Waerenborgh, M.H.R.M. Mendonça, M.R. Nunes, F.M. Costa, Structural and morphological characterization of FeCo2O4 and CoFe2O4 spinels prepared by a coprecipitation method. Sol. State Sci. **5**, 383–392 (2003). https://doi.org/10.1016/S1293-2558(03)00011-6

25. C. Yao, Q. Zeng, G.F. Goya, T. Torres, J. Liu, H. Wu, M. Ge, Y. Zeng, Y. Wang, J.Z. Jiang, ZnFe2O4 nanocrystals: synthesis and magnetic properties. J. Phys. Chem. C **111**, 12274–12278 (2007). https://doi.org/10.1021/jp0732763

26. R. Ramadan, M.K. Ahmed, V. Uskokovic, Magnetic, microstructural and photoactivated antibacterial features of nanostructured Co-Zn ferrites of different chemical and phase compositions. J. All. Comp. **856**, 157013 (2021). https://doi.org/10.1016/j.jallcom.2020.157013

27. F. Gozuak, Y. Koseoglu, A. Baykal, H. Kavasa, Synthesis and characterization of CoxZn1-xFe2O4 magnetic nanoparticles via a PEG-assisted route. J. Magn. Magn. Mater. **321**, 2170–2177 (2009). https://doi.org/10.1016/j.jmmm.2009.01.008

28. S.G.C. Fonseca, L.S. Neiva, M.A.R. Bonifácio, P.R.C. Santos, U.C. Silva, J.B.L. Oliveira, Tunable magnetic and electrical properties of cobalt and zinc ferrites Co1-xZnxFe2O4 synthesized by combustion route. Mater. Res. **21**, e20170861 (2018). https://doi.org/10.1590/1980-5373-MR-2017-0861

29. P.A. Asogekar, S.K. Gaonkar, A. Kumar, V.M.S. Verenkar, Influence of Co over magnetically benign Zn ferrite system and study of its structural, dielectric, superparamagnetic and antibacterial efficacy. Mater. Res. Bull. **141**, 111330 (2021). https://doi.org/10.1016/j.materresbull.2021.111330

30. T. Tatarchuk, M. Bououdina, W. Macyk, O. Shyichuk, N. Paliychuk, I. Yaremiy, B. Al-Najar, M. Pacia, Structural, optical, and magnetic properties of Zn-doped CoFe2O4 nanoparticles. Nanoscale Res. Lett. **12**, 141 (2017). https://doi.org/10.1186/s11671-017-1899-x

31. D. Chahar, S. Taneja, P. Thakur, A. Thakur, Remarkable resistivity and improved dielectric properties of Co–Zn nanoferrites for high frequency applications. J. Alloys. Comp. **843**, 155681 (2020). https://doi.org/10.1016/j.jallcom.2020.155681

32. I. Sharifi, H. Shokrollahi, Nanostructural, magnetic and Mössbauer studies of nanosized Co1−xZnxFe2O4 synthesized by coprecipitation. J. Magn. Magn. Mater. **324**, 2397–2403 (2012). https://doi.org/10.1016/j.jmmm.2012.03.00

33. R.D. Shannon, C.T. Prewitt, Effective ionic radii in oxides and fluorides. Acta Crystallogr. Section B: Struct. Sci Crystal Eng. Mat. **25**, 925–946 (1969). https://doi.org/10.1107/S0567740869003220

34. C.N. Chinnasamy, A. Narayanasamy, N. Ponpandian, K. Chattopadhyay, The influence of Fe3+ ions at tetrahedral sites on the magnetic properties of nanocrystalline ZnFe2O4. Mater. Sci. Eng. A **304–306**, 983–987 (2001). https://doi.org/10.1016/S0921-5093(00)01611-7

35. F.S. Li, L. Wang, J.B. Wang, Q.G. Zhou, X.Z. Zhou, H.P. Kunkel, G. Williams, Site preference of Fe in nanoparticles of $ZnFe_2O_4$. J. Magn. Magn. Mater. **268**, 332–339 (2004). https://doi.org/10.1016/S0304-8853(03)00544-4

36. T. Tatarchuk, A. Shyichuk, Z. Sojka, J. Gryboś, M. Naushad, V. Kotsyubynsky, M. Kowalska, S. Kwiatkowska-Marks, N. Danyliuk, Green synthesis, structure, cations distribution and bonding characteristics of superparamagnetic cobalt-zinc ferrites nanoparticles for Pb(II) adsorption and magnetic hyperthermia applications. J. Mol. Liquids **328**, 115375 (2021). https://doi.org/10.1016/j.molliq.2021.115375

37. S.S. Jadhav, S.E. Shirsath, B.G. Toksha, S.M. Patange, S.J. Shukla, K.M. Jadhav, Structural properties and cation distribution of Co–Zn nanoferrites. Int. J. Modern. Phys. B **23**, 5629–5638 (2009). https://doi.org/10.1142/S021797920905225X

38. G. Fan, J. Tong, F. Li, Visible-light-induced photocatalyst based on cobalt-doped zinc ferrite nanocrystals. Ind. Eng. Chem. Res. **51**, 13639–13647 (2012). https://doi.org/10.1021/ie201933g

39. W.S. Mohamed, M. Alzaid, M.S.M. Abdelbaky, Z. Amghouz, S. García-Granda, A.M. Abu-Dief, Impact of Co2+ substitution on microstructure and magnetic properties of CoxZn1-xFe2O4 nanoparticles. Nanomaterials **9**, 1602 (2019). https://doi.org/10.3390/nano9111602

40. R.S. Yadav, I. Kuritka, J. Vilcakova, P. Urbanek, M. Machovsky, M. Masar, M. Holek, Structural, magnetic, optical, dielectric, electrical and modulus spectroscopic characteristics of $ZnFe_2O_4$ spinel ferrite nanoparticles synthesized via honey-mediated sol-gel combustion method. J. Phys. Chem. Sol. **110**, 87–99 (2017). https://doi.org/10.1016/j.jpcs.2017.05.029

41. R.K. Ahrenkiel, T.J. Coburn, D. Pearlman, E. Carnall, T.W. Martin, S.L. Lyu, A new class of room-temperature magneto-optic insulators: the cobalt ferrites. AIP Conf. Proc. **24**, 186 (1975). https://doi.org/10.1063/1.30040

42. .G.S. Krinchik, A.P. Khrebtov, A.A. Askochenski, E.M. Speranskaya, S.A. Belyaev, Magneto-optical spectra of 3d ions in spinel ferrites and weak ferromagnets. Zh. Eksp. Teor. Fiz. 72, 699–711; Sov. Phys. JETP 45, 366–372 (1977). http://jetp.ras.ru/cgi-bin/dn/e_045_02_0366.pdf

43. .G.S. Krinchik, K.M. Mukimov, S.M. Sharipov, A.P. Khrebtov, E.M. Speranskaya, The permittivity tensor and increase in the transmittance of the spinel ferrites upon their conversion into single-sublattice structures. Zh. Eksp. Teor. Fiz. 76, 2126–2136; Sov. Phys. JETP 49, 1074–1079 (1979). http://jetp.ras.ru/cgi-bin/dn/e_049_06_1074.pdf.

44. Y. Yamazaki, T. Namikawa, K. Suzuki, G. Oda, Preparation of CoZn-ferrite thin films and their magneto-optic properties. IEEE Trans. Magn. **23**, 3320–3322 (1987). https://doi.org/10.1109/TMAG.1987.1065412

45. L. Stichauer, G. Gavoille, Z. Simsa, Optical and magneto-optical properties of nanocrystalline cobalt ferrite films. J. Appl. Phys. **79**, 3645–3650 (1996). https://doi.org/10.1063/1.361192

46. W.F.J. Fontijn, P.J. van der Zaag, R. Metselaar, On the origin of the magneto-optical effects in Li, Mg, Ni, and Co ferrite. J. Appl. Phys. **83**, 6765–6767 (1998). https://doi.org/10.1063/1.367992

47. W.F.J. Fontijn, P.J. Zaag, L.F. Fiener, R. Metselaar, M.A.C. Devillers, A consistent interpretation of the magneto-optical spectra of spinel type ferrites. J. Appl. Phys. **85**, 5100–5105 (1999). https://doi.org/10.1063/1.369091

48. K.J. Kim, H.S. Lee, M.H. Lee, S.H. Lee, Comparative magneto-optical investigation of d–d charge–transfer transitions in Fe_3O_4, $CoFe_2O_4$, and $NiFe_2O_4$. J. Appl. Phys. **91**, 9974–9977 (2002). https://doi.org/10.1063/1.1480482

49. C. Himcinschi, I. Vrejoiu, G. Salvan, A. Talkenberger, D.R.T. Zahn, D. Rafaja, J. Kortus, Optical and magneto-optical study of nickel and cobalt ferrite epitaxial thin films and submicron structures. J. Appl. Phys. **113**, 084101 (2013). https://doi.org/10.1063/1.4792749

50. F. Choueikani, D. Jamon, S. Neveu, M.F. Blanc-Mignon, Y. Lefkir, F. Royer, Self-biased magneto-optical films based on $CoFe_2O_4$–silica nanocomposite. J. Appl. Phys. **129**, 023101 (2021). https://doi.org/10.1063/5.0032620

51. E. Lišková-Jakubisová, Š Višňovský, P. Široký, D. Hrabovský, J. Pištora, S.C. Sahoo, S. Prasad, N. Venkataramani, M. Bohra, R. Krishnan, Nanocrystalline zinc ferrite films studied by magneto-optical spectroscopy. J. App. Phys. **117**, 17B726 (2015). https://doi.org/10.1063/1.4916936

52. W.D. Martens, W.L. Peeters, H.M. Noort, M. Erman, Optical, magneto-optical and Mössbauer spectroscopy on Co3+ substituted cobalt ferrite. J. Phys. Chem. Solids **46**, 411–416 (1985). https://doi.org/10.1016/0022-3697(85)90104-0

53. S.J. Lee, S.H. Song, C.C. Lo, S.T. Aldini, D.C. Jiles, Magneto-optic properties of CoFe2–xGaxO4. J. Appl. Phys. **101**, 09C502 (2007). https://doi.org/10.1063/1.26939535

54. B. Zhou, Y.W. Zhang, Y.J. Yu, C.S. Liao, C.H. Yan, Correlation between structure and intervalence charge-transfer transitions in nanocrystalline CoFe2-xMxO4 (M=Mn, Al, Sc) thin films. Phys. Rev. B **68**, 024426 (2003). https://doi.org/10.1103/PhysRevB.68.024426

55. B.S. Holinsworth, C. Harms, S. Fan, D. Mazumdar, A. Gupta, S.A. McGill, J.L. Musfeldt, Magnetic field control of charge excitations in $CoFe_2O_4$. Apl. Mater. **6**, 066110 (2018). https://doi.org/10.1063/1.5021792

56. Y.A. Gromova, V.G. Maslov, M.A. Baranov, R. Serrano-García, V.A. Kuznetsova, F. Purcell-Milton, Y.K. Gun'ko, A.V. Baranov, A.V. Fedorov, Magnetic and optical properties of isolated and aggregated $CoFe_2O_4$ superparamagnetic nanoparticles studied by MCD. J. Phys. Chem. C **122**, 11491–11497 (2018). https://doi.org/10.1021/acs.jpcc.8b00829

57. S. Wang, H. Onoda, J. Harbovsky, H. Yanagihara, J. Inoue, T. Ishibashi, Magneto-optical spectroscopy of epitaxial CoxFe3-xO4 (001) thin films. J. Magn. Soc. Jap. **47**, 137–143 (2023). https://doi.org/10.3379/msjmag.2311R001

58. Y. Iwasaki, T. Fukumura, H. Kimura, A. Ohkubo, T. Hasegawa, Y. Hirose, T. Makino, K. Ueno, M. Kawasaki, High-throughput screening of ultraviolet–visible magnetooptical properties of spinel ferrite (Zn, Co)Fe2O4 solid solution epitaxial film by a composition-spread approach. Appl. Phys. Exp. **3**, 103001 (2010). https://doi.org/10.1143/APEX.3.103001

59. .A.K. Zvezdin, V.A. Kotov, Modern magnetooptics and magnetooptical materials. (Taylor & Francis Group, New York 1997). https://books.google.ru/books?id=hQ7Xk7MToRoC&printsec=frontcover&hl=ru#v=onepage&q&f=false.

60. E. Prince, Neutron diffraction observation of heat treatment in cobalt ferrite. Phys. Rev. **102**, 674–676 (1956). https://doi.org/10.1103/PhysRev.102.674

61. H.L. Yakel, Determination of the cation site-occupation parameter in a cobalt ferrite from Synchrotron-Radiation diffraction data. J. Phys. Chem. Solids **41**, 1097–1104 (1980). https://doi.org/10.1016/0022-3697(80)90065-7

62. J.W.D. Martens, W.L. Peeters, M. Erman, An ellipsometric and magneto-optical study of cobalt ferrite single crystals. Sol. State Commun. **41**, 667–669 (1982). https://doi.org/10.1016/0038-1098(82)90727-X

63. A. Moskvin, Charge transfer transitions and circular magnetooptics in ferrites. Magnetochemistry **8**, 81 (2022). https://doi.org/10.3390/magnetochemistry8080081

64. V. Zviagin, P. Richter, T. Bontgen, M. Lorenz, M. Ziese, D.R.T. Zahn, G. Salvan, M. Grundmann, R. Schmidt-Grund, Comparative study of optical and magneto-optical properties of normal, disordered, and inverse spinel-type oxides. Phys. Status Solidi B **253**, 429–436 (2016). https://doi.org/10.1002/pssb.201552361

65. J.W.D. Martens, W.L. Peeters, P.Q.J. Nederpel, M. Erman, The polar magnetooptical Kerr effect and the dielectric tensor elements of CoFe2−xAlxO4 0.1≤x≤1 in the photon energy range 0.65≤hv≤4.5 eV. J. Appl. Phys. **55**, 1100–1104 (1984). https://doi.org/10.1063/1.333199

66. .D.T. Sviridov, R.K. Sviridova, Y.F. Smirnov, Optical spectra of the transition metal ions in crystals. (Nauka, Moscow 1976)

67. A.H. Weakliem, Optical Spectra of Ni2+, Co2+, and Cu2+ in tetrahedral sites in crystals. J. Chem. Phys. **36**, 2117–2140 (1962). https://doi.org/10.1063/1.1732840

68. T. Schwab, M. Niedermaier, G. Zickler, M. Oncak, D. Oliver, Isolated cobalt ions embedded in magnesium oxide nanostructures: spectroscopic properties and redox activity. Chem. Eur. J. **26**, 16049–16056 (2020). https://doi.org/10.1002/chem.202002817